Computation of Total and Differential Sputter Yields of Boron Nitride Using Molecular Dynamics

Brandon D. Smith* and Iain D. Boyd†
Nonequilibrium Gas and Plasma Dynamics Laboratory
University of Michigan, Ann Arbor, Michigan, 48109, USA

Abstract: The principal life-limiting mechanism of Hall thrusters is erosion of the discharge channel walls via ion sputtering. Few sputter yield measurements exist for hexagonal boron nitride (hBN), a common wall material, in the range of ion energies of interest to Hall thrusters, and past modeling efforts have had limited success due to the high computational costs associated with sputter modeling. Presented in this work is an updated molecular dynamics model for the sputtering of hexagonal boron nitride by energetic xenon ions. The model uses graphics processing units to accelerate its computations, allowing better statistics to be achieved when calculating the sputter yields. The model is used to simulate hBN sputtering by ions with kinetic energies of 100 eV and 250 eV and incidence angles of 0° and 45°. It is demonstrated that nitrogen is rapidly depleted from the hBN lattice, leaving a boron-enriched layer and causing the total sputter yield to be strongly dependent on ion fluence. Of the four cases tested, only the 100 eV, 45° incidence case appears to be close to a steady state after more than 35,000 ion impacts. Comparisons to experimental measurements by weight loss and quartz crystal microbalance suggest that the 100 eV, 45° incidence case agrees well with existing data. Differential sputter yields are computed and are shown to be well-described by the modified Zhang function. The species composition of the sputtered particles is analyzed, revealing that the most common sputtered species are atomic boron and diatomic nitrogen. Velocity distribution functions for these two species are computed. The VDF of atomic boron normal to the hBN surface is shown to follow a Sigmund-Thompson distribution. The VDF of diatomic nitrogen exhibits a strong bimodal nature and is better described by a superposition of flux-biased Maxwell-Boltzmann distributions.

Nomenclature

a_F	=	Screening length
a_0	=	Bohr radius
$c, d, h, n, S, \beta, \gamma, \lambda$	=	Fitting parameters for Albe potential
D_0, r_0	=	Dimer energy and separation
E	=	Ion kinetic energy
E^*	=	Characteristic energy for modified Zhang fit
E_b	=	Surface binding energy
e	=	Elementary charge
f_c	=	Cutoff function for interatomic potentials
f_{MB}, f_{ST}	=	Maxwell-Boltzmann and Sigmund-Thompson velocity distribution functions
f_R, f_A	=	Repulsive and attractive components of the Albe potential function
GPU	=	Graphics processing unit
hBN	=	Hexagonal boron nitride
k_B	=	Boltzmann constant
LIF	=	Laser-induced fluorescence

* Ph.D. Candidate, Department of Aerospace Engineering, bradenis@umich.edu.
† James E. Knott Professor, Department of Aerospace Engineering, iainboyd@umich.edu.

M_B, M_N = Total mass of boron and nitrogen ejected
MD = Molecular dynamics
MZ = Modified Zhang
m_B, m_N = Mass of boron and nitrogen ejected at a given solid angle
m_{ST}, v_b = Fitting parameters for Sigmund-Thompson velocity distribution function
QCM = Quartz crystal microbalance
R, D = Mean radius and half-thickness of cutoff shell
r_{ij} = Distance separating atoms i and j
T = Temperature
T_0 = Desired equilibrium temperature for Berendsen thermostat
Δt = Time step
v_x, v_y, v_z = Particle velocity in x, y, and z directions
Y = Total or integrated sputter yield, mm^3/C
y = Differential sputter yield, $mm^3/C/sr$
ZBL = Ziegler-Biersack-Littmark
Z_i = Atomic number of atom i
ε_0 = Dielectric permittivity of a vacuum
θ, ϕ = Ejection and azimuthal angles of ejected particles
θ_{ijk} = Angle between atoms i, j, and k
θ_{ion} = Ion incidence angle
λ_B = Velocity scaling factor for Berendsen thermostat
μ_A = Molecular mass of species A
ρ_{hBN} = Mass density of hexagonal boron nitride
τ = Relaxation time for Berendsen thermostat
Φ_{AM} = Albe potential
Φ_{ZBL} = Ziegler-Biersack-Littmark potential
Ω = Solid angle

I. Introduction

THE primary life-limiting mechanism of Hall thrusters is the erosion of the discharge channel walls via sputtering by energetic ions from the plasma. As the walls erode, the magnetic pole pieces are exposed to the plasma and the magnetic topography is changed, ultimately resulting in thruster failure. The erosion process also produces free condensable material that may redeposit in the thruster or on spacecraft surfaces. Hence, characterization of the total erosion rates and transport of the sputtering products can provide valuable information about thruster lifetime and reveal possible spacecraft integration issues.

Historically, Hall thruster operational life has been determined by testing thrusters at high-vacuum conditions until failure occurs. Since such life tests are both time-consuming and expensive, there has been extensive work on describing the erosion process in order to better estimate the lifespan of thrusters without long-term experimental testing. The erosion rate of the discharge channel walls is related to the sputter yield of the wall material, which is a function of the kinetic energy and incidence angle of ions impacting the surface. Some commonly-used wall materials in Hall thrusters are hexagonal boron nitride (hBN) and hBN-based ceramics. While there have been some past efforts at measuring sputter yields of hBN experimentally using techniques such as mass loss,[1–4] cavity ring-down spectroscopy (CRDS),[3] and quartz crystal microbalance (QCM),[5] these efforts have provided limited data in the range of ion energies most important to Hall thruster channel erosion (tens to hundreds of eV) due to sputter yield levels falling below the measurement thresholds of the instruments used. In addition, only the QCM measurements provide detailed differential sputter yield data that could be used to describe the behavior of sputtered particles as they leave the material surface.

The gaps in the experimental data motivated a numerical effort by Yim and Boyd,[6] which used a molecular dynamics (MD) model to simulate the sputtering of hBN by energetic xenon ions. This model appeared capable of calculating total sputter yields of hBN even at low ion energies, but estimating differential sputter yields proved to be infeasible due to the limited computational power available at the time. Recent advancements in computing, however, have made such simulations much more tractable, motivating the development of an updated model.

In this work, we present a new, high-speed MD model for the sputtering of hBN by energetic xenon ions based on the previous work by Yim. In Section II, the details of the model are described, including the basic framework,

the interatomic potentials used, the domain configuration, the simulation progression, and the data reduction procedure. In Section III, the model is used to compute the total and differential sputter yields of hBN for a set of ion energies and incidence angles. Both the total and differential sputter yields are compared to existing experimental data. In addition, the species composition of the sputtered particles is analyzed and velocity distribution functions (VDFs) of the individual sputtered species are computed. Curves are fit to the computed VDFs in order to make comparisons to experimental measurements using laser-induced fluorescence (LIF).[7] Finally, in Section IV, the findings of this work are summarized and the basis for future work is laid out.

II. Numerical model

A. Molecular dynamics framework

The model used in this work applies molecular dynamics (MD) to simulate the sputtering of hBN by xenon ions. MD is a deterministic method for simulating systems at the atomic level. The atoms in the system are assumed to behave as classical particles that obey Newton's laws of motion. Atoms interact with one another through analytical interatomic potential functions. At each time step, the force acting on each atom is computed as the sum of forces from the surrounding atoms. Then, the position and velocity of each atom are integrated forward in time, leading to a new system state.

Several general-purpose MD codes have been developed over the past two decades, such as LAMMPS,[8] GROMACS,[9] NAMD,[10] and DL_POLY.[11] The MD code chosen for use in this work is HOOMD-blue.[‡,12] HOOMD-blue is an open-source code that utilizes Nvidia's CUDA computing architecture[13] to run MD simulations on graphics processing units (GPUs). GPUs were originally developed to perform the massively-parallel floating-point computations required to generate high-fidelity computer graphics. When applied to MD computations, a single high-performance desktop GPU can reduce the wall time of simulations by two or more orders of magnitude. For sputtering simulations, this allows many more ion impacts to be processed in a given amount of time, improving the statistics for both total and differential sputter yield computations. GPUs are also inexpensive, costing only a few hundred US dollars for a high-performance desktop GPU or a few thousand for a GPU designed for scientific computing. Together, the large performance benefits and low cost of GPU computing make HOOMD-blue an ideal MD code for use in the present work.

B. Interatomic potentials

There are two interatomic potentials used in the sputtering model: one for the interactions between the boron and nitrogen atoms in the hBN lattice, and another for the interactions between the impacting xenon ion and the atoms in the lattice. It should be noted that the impacting xenon will henceforth be referred to as the ion for convenience, though it is generally assumed that the ion neutralizes upon impact.

To model the interactions between the boron and nitrogen atoms in the lattice, HOOMD-blue uses a Tersoff-like three-body potential developed by Albe, Möller, and Heinig for boron nitrides.[14, 15] This is a bond-order potential, and thus accounts for factors such as the number of bonded neighbors, the bond lengths, and the bond angles between multiple atoms. It takes the form

$$\Phi_{AM} = \frac{1}{2}\sum_{i \neq j} f_c(r_{ij})\left[f_R(r_{ij}) + b_{ij} f_A(r_{ij})\right], \tag{1}$$

where the repulsive and attractive terms take the form of a Morse potential:

$$\begin{aligned} f_R(r) &= \frac{D_0}{S-1}\exp\left(-\beta\sqrt{2S}(r-r_0)\right), \\ f_A(r) &= \frac{SD_0}{S-1}\exp\left(-\beta\sqrt{2/S}(r-r_0)\right). \end{aligned} \tag{2}$$

The coefficient b_{ij} is a modifier term that accounts for the number of bonded neighbors and enforces bond angles between three or more atoms. It has the form

‡ HOOMD-blue web page: http://codeblue.umich.edu/hoomd-blue

$$b_{ij} = \left(1 + \gamma^n \chi_{ij}^n\right)^{-\frac{1}{2n}},$$

$$\chi_{ij} = \sum_{k \neq i,j} f_c(r_{ik}) g\left(\theta_{ijk}\right) \exp\left(\lambda^3 \left(r_{ij} - r_{ik}\right)^3\right), \tag{3}$$

$$g\left(\theta_{ijk}\right) = 1 + \frac{c^2}{d^2} - \frac{c^2}{d^2 + \left(h - \cos\theta_{ijk}\right)^2}.$$

The cutoff function f_c limits the interaction range between atoms by smoothly transitioning the potential to zero at some finite distance. The function used in this work is based on an exponential[6,16]:

$$f_c(r) = \begin{cases} 1, & r \leq R - D \\ \exp\left(\frac{3\hat{r}^3}{\hat{r}^3 - 1}\right), & R - D < r < R + D \\ 0, & r \geq R + D \end{cases}, \tag{4}$$

$$\hat{r} = \frac{r - (R - D)}{2D}.$$

Table 1 shows the values of all of the Albe parameters for B–B, B–N, and N–N interactions. The parameters are dependent only on the species of atoms i and j, not on the species of the tertiary atoms k. Note that the values of c and d for the B–B interactions differ from those found by Albe. Yim determined that the original values resulted in a very high sensitivity to the bond angle about the critical angle determined by h. This high sensitivity requires a very small time step in order to resolve the particle motion, so Yim modified the values to maintain the same ratio c^2/d^2 while reducing the sensitivity to the bond angle. Since B–B bonds do not occur in bulk BN, it is unclear whether this will have any adverse effects on the sputter yield computations.

The potential used to model the interactions of the covalently-bonded boron and nitrogen with the impacting ion is the Ziegler-Biersack-Littmark (ZBL) "universal" potential.[17] This is a screened Coulomb potential of the form

$$\Phi_{ZBL}\left(r_{ij}\right) = \frac{Z_i Z_j e^2}{4\pi\varepsilon_0 r_{ij}} \phi_{ZBL}\left(\frac{r_{ij}}{a_F}\right),$$

$$\phi_{ZBL}(x) = \sum_{k=1}^{4} A_k \exp(-B_k x), \tag{5}$$

$$a_F = \frac{0.8853 a_0}{Z_i^{0.23} + Z_j^{0.23}}.$$

The values for A_k and B_k are shown in Table 2. This potential differs slightly from the Molière potential used by Yim. While both the ZBL and Molière potentials are screened Coulomb potentials, they use different definitions for the screening length a_F, and the Molière screening function contains fewer terms. However, the ZBL potential better matches effective screening functions gathered from scattering experiments.[18] The ZBL potential has also been used in other MD studies

Table 1. Albe potential parameters for B–B, B–N, and N–N interactions.

	B–B	B–N	N–N
D_0, eV	3.08	6.36	9.91
r_0, Å	1.59	1.33	1.11
S	1.0769	1.0769	1.0769
β, Å^{-1}	1.5244506	2.043057	1.92787
γ	1.6×10^{-6}	1.1134×10^{-5}	1.9251×10^{-2}
n	3.9929061	0.364153367	0.6184432
λ, Å^{-1}	0	1.9925	0
c	3.316257	1092.9287	17.7959
d	0.01	12.38	5.9484
h	0.5	-0.5413	0
R, Å	2.0	2.0	2.0
D, Å	0.1	0.1	0.1

Table 2. Coefficient values for the ZBL potential.

k	1	2	3	4
A_k	0.1818	0.5099	0.2802	0.02817
B_k	3.2	0.9423	0.4029	0.2016

Table 3. Lattice constants for hBN.[14]

Lattice constant	Length, Å
a	2.496
c	3.245
s	1.441

concerning hBN, as has the Albe potential described above.[15, 19] For these reasons, it was deemed appropriate to substitute the ZBL potential for the Molière potential.

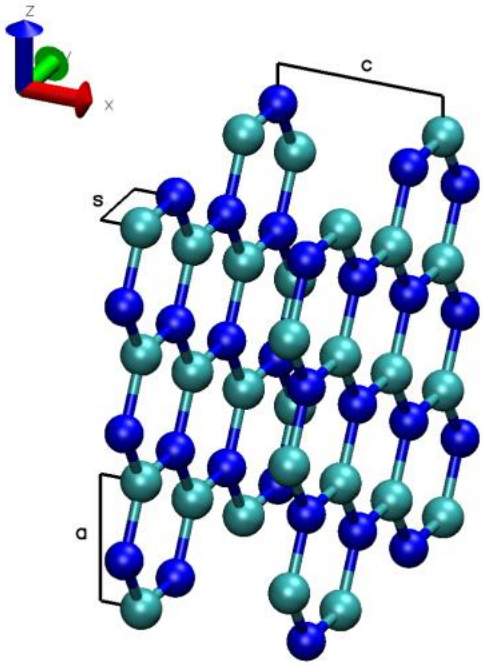

Figure 1. Sample domain for sputtering simulations with definitions for the lattice constants a, c, and s. Boron atoms are green, nitrogen atoms are blue. Graphic generated using VMD software.[20]

C. Domain configuration and simulation progression

The domain for the MD simulations consists of a single lattice of hBN. A small sample domain is shown in Fig. 1. The xy-plane defines the surface plane of the hBN sample, and the z-axis defines the surface normal vector. The domain size is set by the numbers of graphene-like sheets, point-to-point hexagons, and side-to-side hexagons. The size of the hexagons is determined by the lattice constants a and s, and the spacing between sheets is determined by the lattice constant c. The three lattice constants are defined in Fig. 1 and their values are shown in Table 3. Periodic boundary conditions are used along the x and y axes. The boundaries along the z-axis are open, allowing particles to pass through them and exit the domain. Since the simulated lattice represents a depth of only a few angstroms at the surface of a much larger hBN sample, the bottommost boron and nitrogen atoms (i.e., those with the smallest z positions) are fixed in place. This represents the mechanically-stabilizing effect of the greater hBN sample, maintaining zero net momentum for the simulated lattice. The two layers of atoms just above the immobile layer are dubbed the thermostat layers and regulate the system temperature. The thermostat layers serve to dissipate the energy deposited by an impacting ion after that energy diffuses away from the surface. This is accomplished via a Berendsen thermostat, which rescales atom velocities according to the system temperature:[21]

$$\lambda_B = \sqrt{1 + \frac{\Delta t}{\tau}\left(\frac{T_0}{T} - 1\right)}. \tag{6}$$

For the current work, two domain sizes are used. For the 100 eV simulations, an initial domain consisting of 32 sheets of 12 side-to-side hexagons and 24 point-to-point hexagons is used. For the 250 eV simulations, the initial domain consists of 40 sheets of 12 side-to-side hexagons and 30 point-to-point hexagons. Additional hexagons are added to the bottom of the domain as the surface atoms sputter away. This prevents the surface from being eroded to the point where the thermostat and immobile atom layers interfere with the collision dynamics at the ion impact site.

Ion impacts are simulated by placing an ion above the hBN lattice with a given kinetic energy and incidence angle. The incidence angle is defined as the angle between the ion's velocity vector and the surface normal such that an incidence angle of 0° corresponds to normal incidence. The ion's initial position in the xy-plane and the azimuth of its velocity vector are randomized in order to minimize the influence of lattice orientation on the resulting sputter yields. The initial velocities of the lattice atoms are sampled from a Maxwell-Boltzmann distribution at the desired equilibrium temperature T_0. The position and velocity of each particle are integrated using a second-order velocity-Verlet scheme with a time step of 0.1 fs. The species and center-of-mass velocity of all atoms and molecules passing a z-boundary are recorded to a text file for post-processing. After each ion impact, the system is allowed to reach a thermal equilibrium defined by $T = T_0$ before another ion is injected. The equilibrium temperature T_0 is set to 150°C in order to match the sample temperature reported in sputtering

experiments.[1, 3] The system temperature T is monitored using a sub-relaxation technique[22] in order to minimize the effects of instantaneous temperature fluctuations. Unless otherwise noted, all simulations begin with a perfect hBN lattice. Additional ions are injected after each impact until the average sputter yield reaches a steady state. A steady-state sputter yield is defined by two criteria:

1. The total ejection rate of nitrogen atoms is equal to that of boron atoms on average.
2. The average sputter yield does not change with increasing ion fluence.

The importance of the first criterion is discussed in detail in Section III-A.

D. Data reduction

For each ion impact, HOOMD-blue outputs the time of ejection, species, kinetic energy, and the ejection and azimuthal angles of the velocity vector of each particle (atom or molecule) that passes a z boundary. The ejection angle is defined as the angle between the particle's velocity vector and the surface normal of the lattice such that an ejection angle of 0° corresponds to a particle leaving the domain normal to the lattice surface (along the z-axis in Fig. 1). These data must be reduced in order to find total sputter yields, differential sputter yields, and velocity distribution functions (VDFs). The total sputter yield averaged over some number of ion impacts N can be written as:

$$Y = \frac{M_B + M_N}{Ne\rho_{hBN}}. \tag{7}$$

Differential sputter yields are computed by generating a virtual hemisphere centered at the origin of the ejected particle and separating its surface into sections of equal solid angle Ω. The differential sputter yield at a given solid angle is then

$$y(\theta,\phi) = \frac{m_B(\theta,\phi) + m_N(\theta,\phi)}{Ne\Omega\rho_{hBN}}, \tag{8}$$

where θ and ϕ define the centroid of the solid angle Ω. For comparison to experimental data, a modified Zhang (MZ) function is fit in a least-squares sense to the computed differential yields:[23, 24]

$$\begin{aligned} y_{MZ} &= \frac{Y}{1-\sqrt{\frac{E^*}{E}}\cos(\theta_{ion})} \times \frac{\cos(\theta)}{\pi} \\ &\times \left[1 - \frac{1}{4}\sqrt{\frac{E^*}{E}}\left(\cos(\theta_{ion})\,\psi(\theta) + \frac{3}{2}\pi\sin(\theta_{ion})\sin(\theta)\cos(\phi)\right)\right], \end{aligned} \tag{9}$$

$$\psi(\theta) = \frac{3\sin^2(\theta)-1}{\sin^2(\theta)} + \frac{\cos^2(\theta)\,(3\sin^2(\theta)+1)}{2\sin^3(\theta)} \times \ln\left(\frac{1+\sin(\theta)}{1-\sin(\theta)}\right),$$

with $\phi = 0$ corresponding to the forward sputtering direction.

VDFs are computed from the raw data by separating velocity space into bins and allocating the ejected particles into the appropriate bins. This is done independently for each species represented in the population of ejected particles. Curves are then fit to the computed histograms. The exact function used to fit to the data depends on the axis under consideration. For the x and y directions, a Maxwell-Boltzmann distribution is fit to the computed VDFs. For the z direction, one of two functions is used. The first is the flux-based form of the Sigmund-Thompson distribution:[25, 26]

$$f_{ST}(v_z) \propto \frac{v_z^3}{(v_z^2 + v_b^2)^{3-2m_{ST}}} \tag{10}$$

where v_b is the velocity corresponding to the surface binding energy, $E_b = \mu_B v_b^2/2$. This function has been used in the past to describe the velocity distribution of boron atoms sputtered from an hBN target.[7] The second fitting function for the z direction is the flux-shifted Maxwell-Boltzmann distribution:

$$f(v_z) \propto v_z \exp\left(-\frac{\mu v_z^2}{2k_B T}\right). \quad (11)$$

where T is treated as a fit parameter. Note that both of the functions used to fit the z velocities are flux-based due to the way the particle data are recorded.

III. Results and discussion

A. Total sputter yields

1. Dependence on ion fluence

Figure 2 shows the total average sputter yield as a function of total ion fluence for the four cases simulated in this work. Note that the 250 eV, normal incidence case uses an initial lattice that is pre-battered by several thousand 250 eV ions at 45° incidence. The values plotted are cumulative averages for the first 8000 impacts and are moving averages with an interval of 8000 ion impacts thereafter.

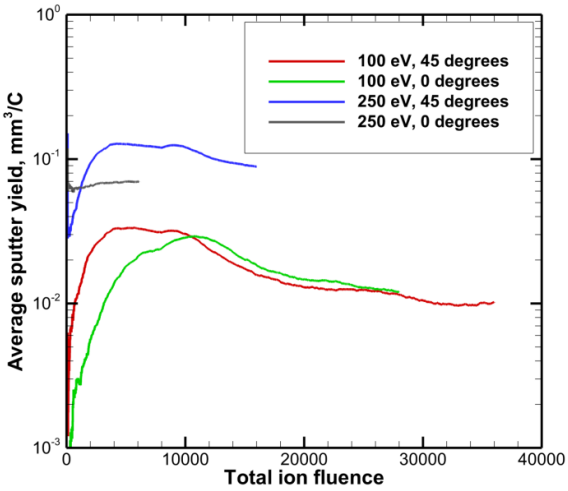

Figure 2. Total sputter yield as a function of total ion fluence.

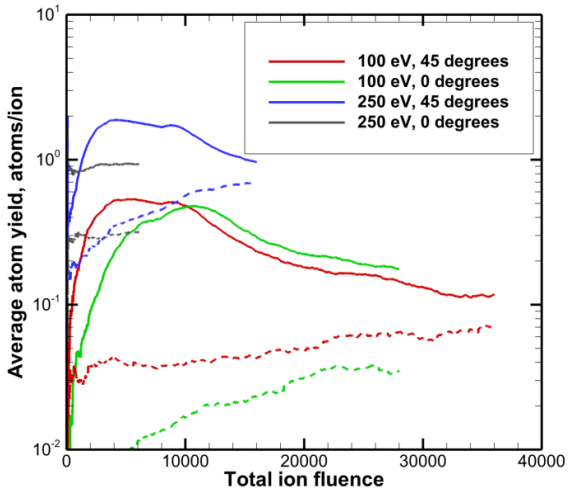

Figure 3. Atomic yield of nitrogen and boron in sputtering simulations. Solid lines represent nitrogen and dashed lines represent boron.

For the three cases that begin with a perfect hBN lattice, the average sputter yields increase over the first several thousand ion impacts before appearing to reach a plateau. This is caused by the deformation of the crystal structure at the hBN surface, resulting in an amorphous region. After that, however, the sputter yields begin to fall. The initial rise in the sputter yield is consistent with Yim's observations,[18] but Yim's simulations did not proceed past a total fluence of 1500 ions, so it is not clear whether a similar decrease in the sputter yields would have manifested in his data. The physical cause of such a decrease in the sputter yields is also unclear, but is likely related to the species composition of the ejected particles. Figure 3 shows the total number of nitrogen and boron atoms ejected per ion, including those ejected as molecules, as a function of ion fluence. For all four cases, nitrogen is sputtered preferentially over boron. In fact, over the first several thousand ion impacts, nitrogen is sputtered at approximately ten times the rate of boron, suggesting that nitrogen is rapidly depleted from the surface layers of the lattice. This causes apparent boron enrichment in the surface layers, a phenomenon observed by Yim in his simulations.[6] As the nitrogen is depleted from the surface layers and more pure boron is exposed, nitrogen becomes less likely to be ejected from the system, resulting in a drop in its atomic yield. This decrease in the atomic yield corresponds to the decrease in the total sputter yield seen in Fig. 2. Meanwhile, the ejection rate of boron increases steadily with increasing ion fluence in all cases. Since the rates of ejection of the two species are not equal, the first of the two steady-state criteria defined in Section II-C is not met and a steady state has not yet been reached.

As previously stated, the initial rise in the sputter yield is likely caused by deformation of the crystal structure at the hBN surface. This same phenomenon can also explain the initial increase in the nitrogen sputtering rate and the steady increase in the boron sputtering rate, but it does not explain why nitrogen is sputtered preferentially. The high rate of ejection of nitrogen is better explained by the form of the Albe potential, defined in Eqs. (1), (2), and (3) with coefficients defined in Table 1. As indicated by Eqs. (1) and (2), the dimer energy D_0 determines the depth of

Table 4. Mole fraction of nitrogen-containing species in the sputtered particle population.

Ion energy	Ion incidence	Monatomic	Diatomic
100 eV	0°	12.1%	81.4%
	45°	19.1%	73.2%
250 eV	0°	12.8%	80.0%
	45°	20.6%	67.9%

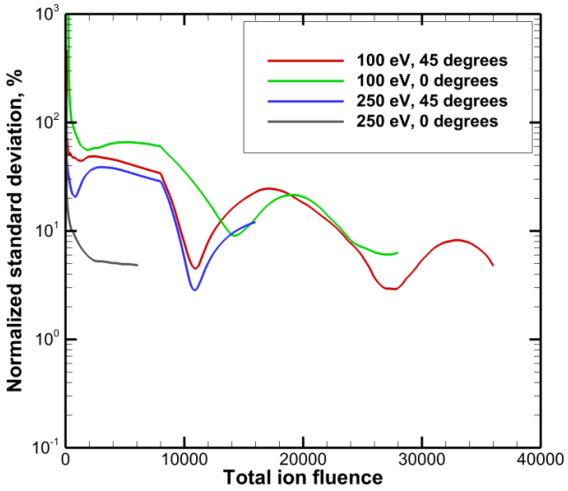

Figure 4. Normalized standard deviation of the total sputter yields.

the potential well for a given ij interaction. Table 1 shows that the dimer energy of 9.91 eV for N–N bonds is greater than that of B–B and B–N bonds. In other words, nitrogen prefers to bond with nitrogen in order to reach a minimum-energy state. This is the reason nitrogen gas is chemically nonreactive. Though no N–N bonds exist in bulk hBN, it is likely that such bonds are formed during an ion impact event when the lattice is compressed and existing bonds are broken. Once such a bond is formed, it is unlikely to break due to its high dimer energy. In addition, such a bond is likely to result in a free N_2 molecule due to the exponential term in Eq. (3). This term reduces the attractive force between two neighboring atoms i and j if there is some atom k such that $r_{ik} < r_{ij}$. N–N bonds have a relatively short dimer separation (see Table 1), so it is unlikely that either nitrogen atom will have any neighbors in closer proximity than its bond partner. Hence, when N–N bonds form in the lattice, the likely product is an N_2 molecule that is free to diffuse out of the domain.

If the above hypothesis is true, then one would expect to see the majority of sputtered nitrogen leave the simulation domain in the form of N_2. To investigate whether this is the case, the mole fractions of nitrogen-containing species ejected from the domain are computed and shown in Table 4. The remaining nitrogen is ejected as BN, metastable N_3 molecules, or larger compounds of B and N. As Table 4 shows, the overwhelming majority of the nitrogen mass lost by the hBN lattice is lost as N_2. This supports the conclusion that fall in the total hBN sputter yield after several thousand ion impacts is a result of rapid nitrogen depletion in the surface layers of the lattice due to the formation of N–N bonds. Interestingly, the mole fraction ejected as N_2 seems to be dependent only on ion incidence angle. Ions at normal incidence probably penetrate deeper into the lattice on impact, allowing them to interact with nitrogen atoms that are buried too deep for ions at oblique incidence to reach. More data need to be collected, however, before any firm conclusions can be drawn.

Given that nitrogen is rapidly depleted from the surface layers of the hBN lattice, it may be valuable to reevaluate the coefficients used for B–B interactions in the Albe potential. As stated in Section II-B, some of the coefficients used for the B–B interactions were modified in order to reduce the sensitivity of such interactions to bond angles with tertiary atoms. This was justified by noting that B–B bonds do not occur in bulk BN. However, as nitrogen is depleted from the MD system, B–B bonds become much more common, perhaps motivating the use of the coefficients proposed by Albe, Möller, and Heinig. Unfortunately, attempts to do so resulted in the system temperature becoming unstable and rising rapidly with time, even when the time step was reduced by two orders of magnitude. Hence, exploring the use of the original Albe coefficients is left for future work.

While it is clear that the first of the two steady-state criteria is not yet met, it may be possible that the ejection rates of boron and nitrogen are changing with ion fluence in such a way that the total sputter yield is approximately constant. If that is the case, then the total sputter yields can be reliably recorded. In order to assess this, one can compute the normalized standard deviation of the total sputter yield (i.e., the standard deviation normalized by the mean) over some number of ion impacts. When this parameter falls below some set value and remains there for a set number of impacts, the sputter yield is said to be constant with increasing ion fluence.

The normalized standard deviation of the average sputter yield is shown in Figure 4 for each case. The plotted values are computed using the moving average interval of 8000 impacts. The normalized standard deviation exhibits an overall trend of decreasing with increasing ion fluence. The 100 eV, 45° incidence case, in particular, maintains a standard deviation of less than 10% for the last 10,000 impacts. Though the total sputter yield for that case may continue to change with continued ion fluence, it is unlikely to undergo any substantial, rapid change unless there is some radical disturbance to the system. Hence, even though the first of the two steady-state criteria is

Table 5. Total sputter yields computed by HOOMD-blue.

Ion energy	Ion incidence	Sputter yield
100 eV	0°	0.0120 ± 0.0008 mm^3/C
	45°	0.0101 ± 0.0008 mm^3/C
250 eV	0°	0.0696 ± 0.0026 mm^3/C
	45°	0.0887 ± 0.0027 mm^3/C

not yet met, the 100 eV, 45° incidence case is treated as though it has reached a steady state for the remainder of this work.

2. Comparison to experiment

Though most of the cases examined in this work have not yet reached a steady state, it is still valuable to compare the computed sputter yields to experimental measurements in order to evaluate qualitative trends. Quantitative comparisons between the numerical and experimental datasets will become more feasible as more cases are simulated to a steady state.

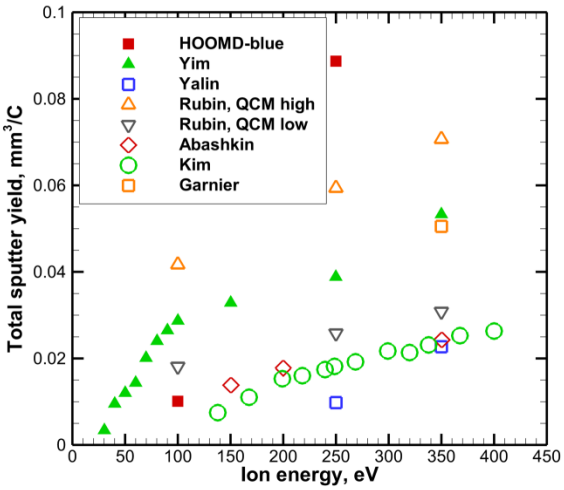

Figure 5. Sputter yields of hBN as a function of ion energy at 45° incidence.

Table 5 shows the total sputter yields computed by HOOMD-blue for the four cases simulated in the present work. The uncertainties given are 95% confidence intervals over the most recent 8000 ion impacts. Note that the sputter yields for the 250 eV cases are greater than those for the 100 eV cases, as expected based on experimental observations.[1–5] At 250 eV, the normal incidence case gives a total sputter yield less than that at 45° incidence, but the 100 eV cases show the opposite trend. Experimental measurements and the previous work by Yim show that the hBN sputter yield at a given ion energy increases with increasing ion incidence until it reaches a peak between 50° and 80° incidence.[1–3, 5, 6] After that, the sputter yield rapidly decreases as the incidence angle approaches 90°. Thus, it appears that the 250 eV sputtering simulations agree with the experimentally-observed dependence of sputter yield on ion incidence angle, but the 100 eV simulations do not. Recall, however, that most of the simulated cases have not yet reached a steady state. It is expected that the sputter yield computed for 100 eV ions at normal incidence will continue to decrease, eventually settling at a total sputter yield less than that at 45° incidence.

Figure 5 shows the sputter yields computed using HOOMD-blue at 45° incidence along with experimental data from various sources, including weight loss data from Garnier,[1] Kim,[2] Yalin,[3] and Abashkin,[4] QCM data from Rubin,[5] and simulation values from Yim.[6] It should be noted that there are two sets of data points for the QCM. The first, labeled QCM high, is the QCM measurement corrected to account for non-condensable species such as N_2. The second, labeled QCM low, is the raw QCM measurement. Both sets are included because the corrected QCM measurements are unusually high compared to the mass loss measurements, as noted by the experimenters.[5] The measurements by Garnier, Yalin, and Rubin are of particular interest due to the high-purity boron nitrides used in those experiments: pyrolytic hBN for Garnier, and HBC-grade boron nitride for Yalin and Rubin . Note that HOOMD-blue predicts a sputter yield at 100 eV that appears to coincide very well with the mass loss measurements by Yalin, Abashkin, and Kim. However, the sputter yield at 250 eV appears to be far too high. As has been stated, this case has not yet reached a steady state. As the case approaches its steady state, the agreement between the computed sputter yield and the measured yields is expected to improve.

B. Differential sputter yields

In computing the differential yields from the raw data, it is assumed that the transient behavior of the total sputter yields does not influence the shape of the differential sputter yield contours. Hence, for the purpose of computing the differential sputter yields, the cumulative average of the sputter yield over all ion impacts is used as the total yield rather than the moving averages reported in Section III-A. This helps to improve the resolution of the computed contours by allowing all ejected particles to be counted. Equation (9) is then fitted to the data for comparison to QCM measurements by Rubin.[5] Since the QCM measures differential yields directly, Rubin treated total yield Y in Eq. (9) as a fit parameter along with the characteristic energy E^*. In the present work, the total sputter yields are known, so only E^* is treated as a fit parameter. Since E^* influences the shape of the differential

sputter yield contours and the shape of the contours is assumed to be independent of ion fluence, it follows that E^* is assumed to be independent of ion fluence, as well.

Figure 6 shows computed differential sputter yield contours and MZ fits for the two 100 eV sputtering simulations. In these plots, the positive x-axis indicates the direction of forward sputtering and the positive z-axis is the surface normal vector. First note that the computed yields are very well resolved even before applying the MZ fit. The case of normal incidence results in differential sputter yield contours that are nearly azimuthally symmetric, as expected from both theory and observation.[5, 23, 27, 28] The 45° incidence case gives contours that are biased toward the forward sputtering direction, again as expected. Fitting the MZ function to the computed yields helps to smooth out any irregularities, but also slightly changes the characteristics of the differential sputter yield contours. Namely, the MZ fits suggest that more particles are ejected at oblique angles relative to the surface normal than do the raw differential yields. Also, because the total sputter yield is the same between the computed yields and the fitted contours, the fits necessarily predict that fewer particles are ejected at near-normal angles. The differences are not dramatic, however: The RMS difference between the raw and fitted contours is about 5–6% of the total yield for both cases, suggesting that the fits describe the raw data very well.

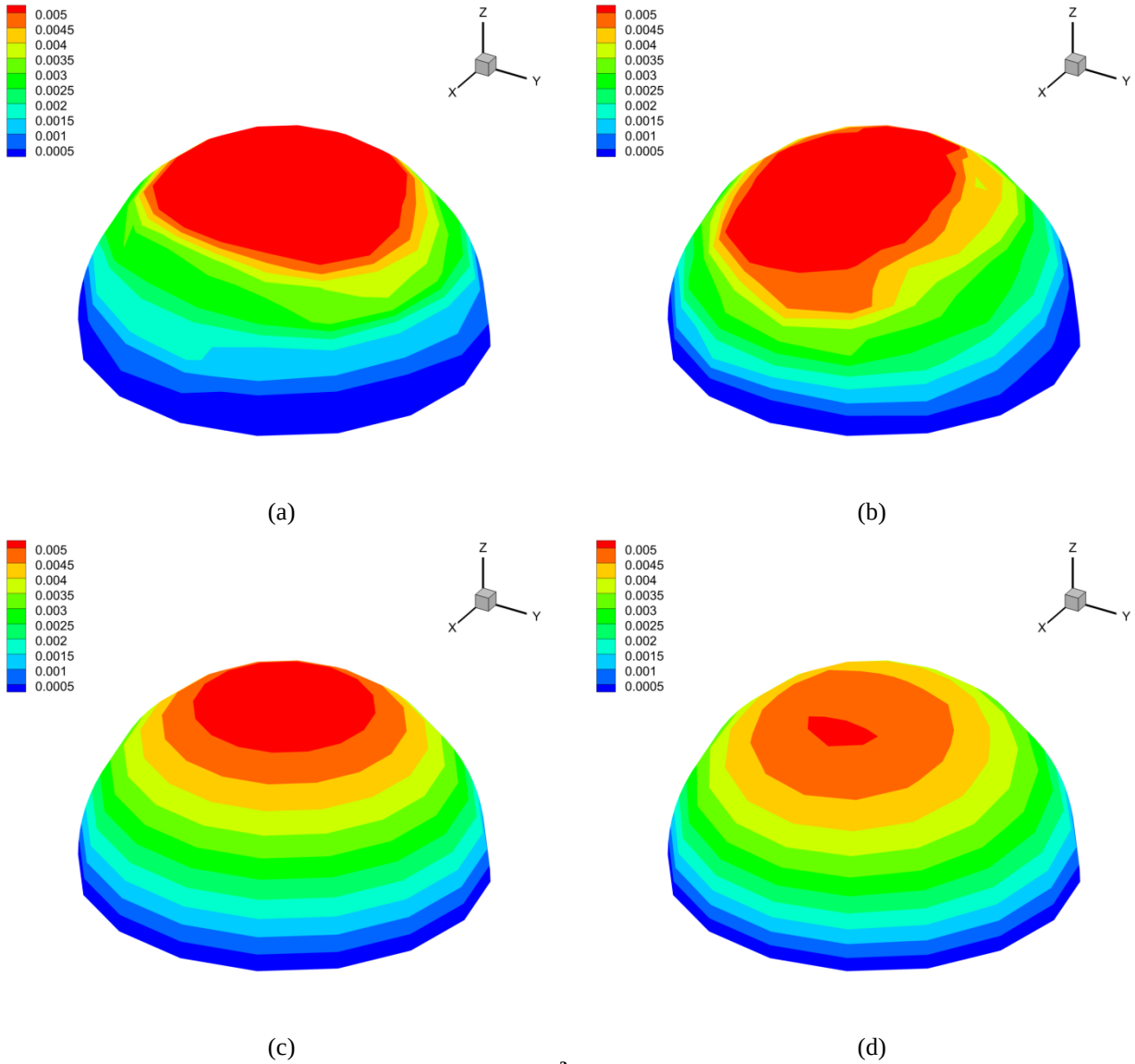

Figure 6. Computed differential sputter yields (mm^3/C/sr) for the 100 eV cases: computed profiles for (a) normal incidence and (b) 45° incidence and modified Zhang fits for (c) normal incidence and (d) 45° incidence.

Figure 7 shows the computed and fitted differential sputter yield contours for the 250 eV cases. The trends seen here are very similar to those seen at 100 eV: The normal incidence case gives contours that are azimuthally symmetric and the 45° incidence case gives contours biased in the direction of forward sputtering. The effects of the MZ fit on the contours are also similar, with more particles ejected at oblique angles and fewer at near-normal angles. The RMS difference for these cases is slightly less than for 100 eV at about 4–5% of the total yield, supporting the conclusion that the MZ fit describes the computed differential sputter yields quite well.

Table 6 shows the values of E^*/E from the MZ fits to

Table 6. E^*/E values for modified Zhang fits to HOOMD-blue data and QCM data by Rubin.

Ion energy	Ion incidence	E^*/E HOOMD-blue	QCM
100 eV	0°	0.0	0.18
	45°	0.06	0.21
250 eV	0°	0.0	0.25
	45°	0.05	0.34

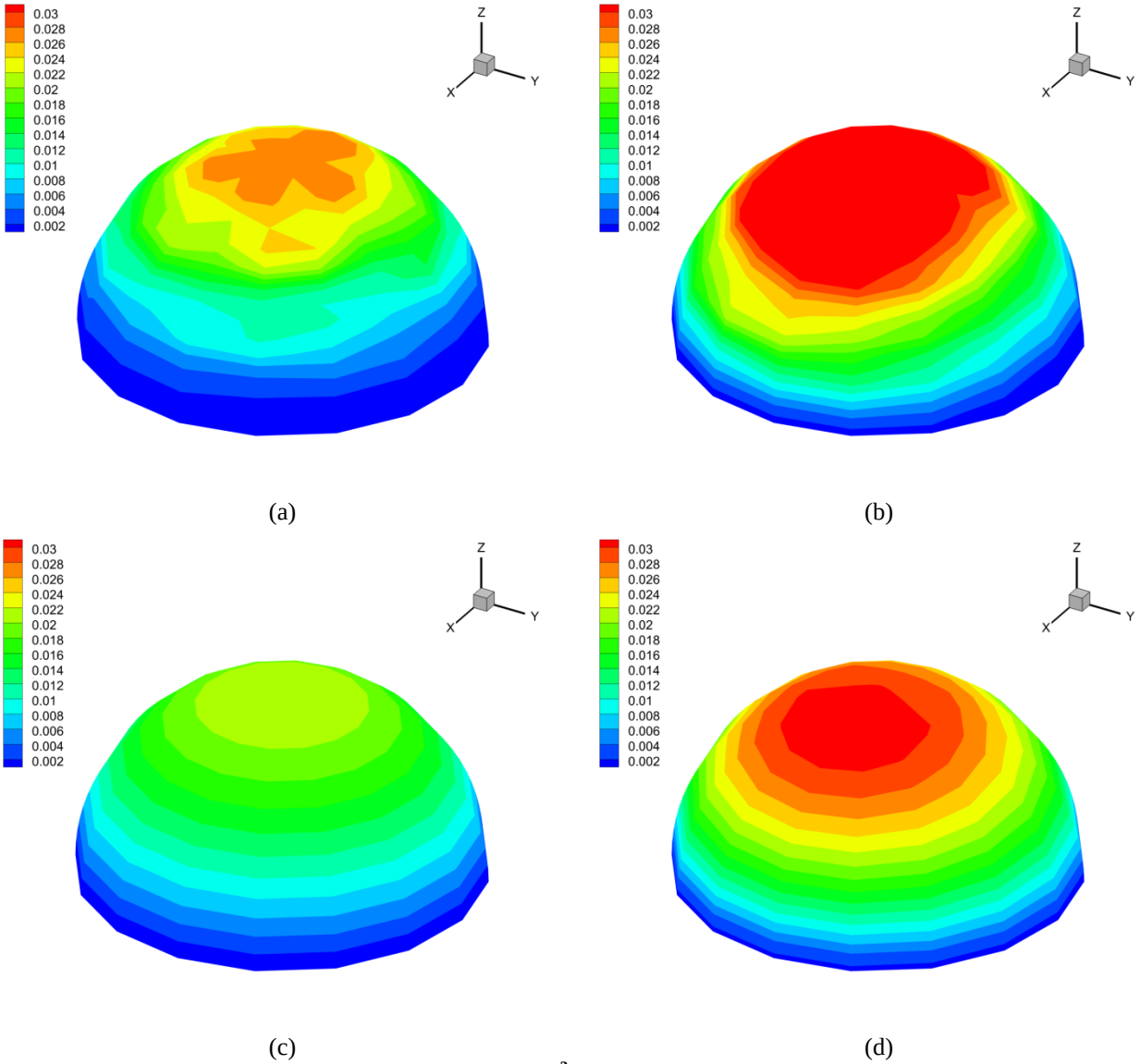

Figure 7. Computed differential sputter yields (mm^3/C/sr) for the 250 eV cases: computed contours for (a) normal incidence and (b) 45° incidence and modified Zhang fits for (c) normal incidence and (d) 45° incidence.

the HOOMD-blue data and to the QCM data from Rubin.[5] The total yield values are omitted since they are compared in Section III-A. While the values do not agree well between the simulations and the experiment, the dependence of E^*/E on the ion incidence angle appears to match. Both the simulations and the experiment suggest that oblique incidence angles result in a larger E^*/E than near-normal incidence angles. This trend appears very consistently in the experimental data,[5] so the fact that it appears to be replicated by the simulations is promising. It is possible that this is a coincidence, however, given the limited simulation dataset available at this time. As more cases are simulated, the dependence of E^*/E on the ion incidence angle can be revisited.

Table 7. Mole fraction of boron-containing species in the sputtered particle population.

Ion energy	Ion incidence	Monatomic	BN	B_i, $i \geq 2$
100 eV	0°	78.1%	18.1%	1.8%
	45°	76.6%	14.7%	7.5%
250 eV	0°	83.5%	10.0%	6.8%
	45°	71.1%	16.2%	11.8%

1. Velocity distribution functions

1. Atomic boron

Table 4 suggests that the majority of nitrogen ejected from the MD system leaves the domain in the form of N_2. The form of sputtered boron, however, has not yet been discussed. Boron and boron compounds are condensable materials, making them especially important when considering how erosion in Hall thrusters can impact spacecraft integration. Table 7 shows the mole fraction of boron-containing species sputtered in the MD simulations. For the four cases simulated in this work, the majority of boron is ejected from the domain in monatomic form. This is consistent with x-ray photoelectron spectroscopy analysis performed by Rubin.[5] Though the other species are also present in significant quantities, the total number of molecules ejected for those species does not give a large enough sample size for computing well-resolved VDFs. Hence, it will be assumed hereafter that boron is sputtered predominantly in its monatomic form.

Figure 8 shows the computed and fitted VDFs for sputtered atomic boron for the 100 eV cases and Fig. 9 shows those for the 250 eV cases. For all cases, the x and y VDFs are fitted using a bimodal Maxwell-Boltzmann distribution rather than a single Maxwellian:

$$f(v) = \sigma f_{MB1}(v) + (1-\sigma) f_{MB2}(v). \tag{12}$$

The VDFs in z are fitted using the Sigmund-Thompson distribution described by Eq. (10). As with the differential sputter yield contours, the positive x-axis corresponds to the direction of forward sputtering and positive z corresponds to the lattice normal vector. For all four cases, the fitted distributions describe the data extremely well; the RMS difference between the computed VDFs and the fits is on the order of 11% or less of the peak value for each case. Of particular note is the z direction, as the computed VDFs reproduce the Sigmund-Thompson distribution predicted by the linear-cascade theory of atomic sputtering.[25, 26] There is some disagreement between the computed VDFs and the fits in the high-energy tail of the distribution, but otherwise the two match very well. The Sigmund-Thompson distribution has also been measured experimentally for atomic boron sputtered from hBN.[7] Past efforts at modeling hBN sputtering at low ion energies have not been able to replicate this distribution, largely due to the high computational cost of such simulations. The high-performance GPU computing used in this work is an enabling factor in generating these high-resolution VDFs.

The VDFs in the x and y directions do not follow the Sigmund-Thompson distribution, but they do exhibit some noteworthy characteristics. First, for the cases of normal incidence, the VDFs in x (Figs. 8a and 9a) are approximately symmetric about zero. This is to be expected since ions at normal incidence should produce azimuthally symmetric sputter yield profiles. At 45° incidence (Figs. 8b and 9b), those VDFs are biased towards a positive velocity in x. Since ions at oblique incidence tend to cause forward sputtering, the forward bias in those VDFs is expected. On the other hand, the VDFs in y are symmetric for all four cases, which is anticipated given the inherent symmetry of the sputtering problem. The most curious result from Figs. 8 and 9 is that the VDFs in x and y appear to have bimodal characteristics, especially in the x direction for oblique ion incidence. These characteristics do not appear in the VDFs in z. The modes are not very distinct, however, so this may only be an indication that the Maxwellian distributions fit to the data do not provide a physically-accurate description of the sputtered boron atoms.

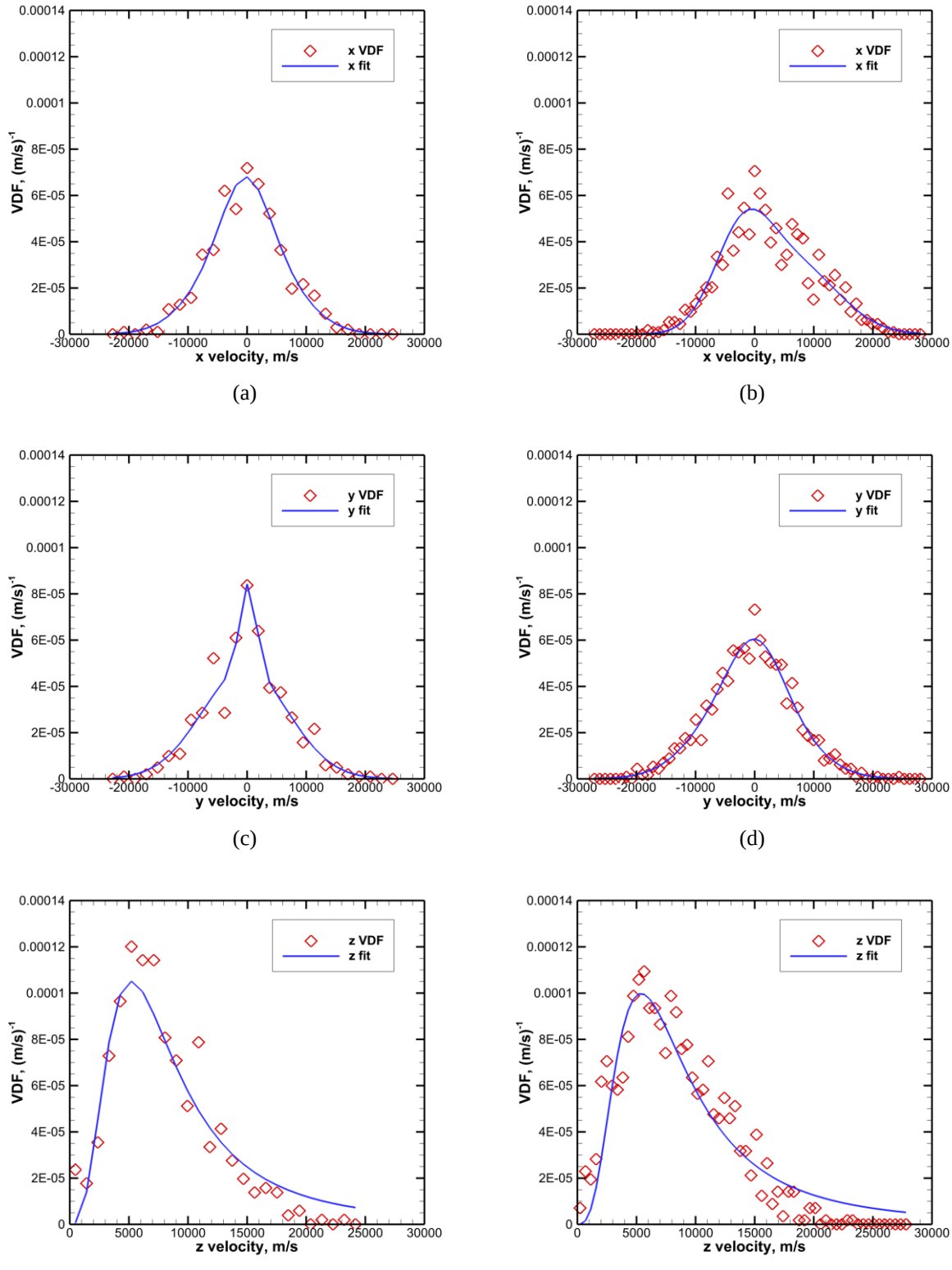

Figure 8. VDFs of atomic boron for 100 eV incident ion energy. The 0° incidence case is on the left-hand side of the page and the 45° incidence case is on the right-hand side.

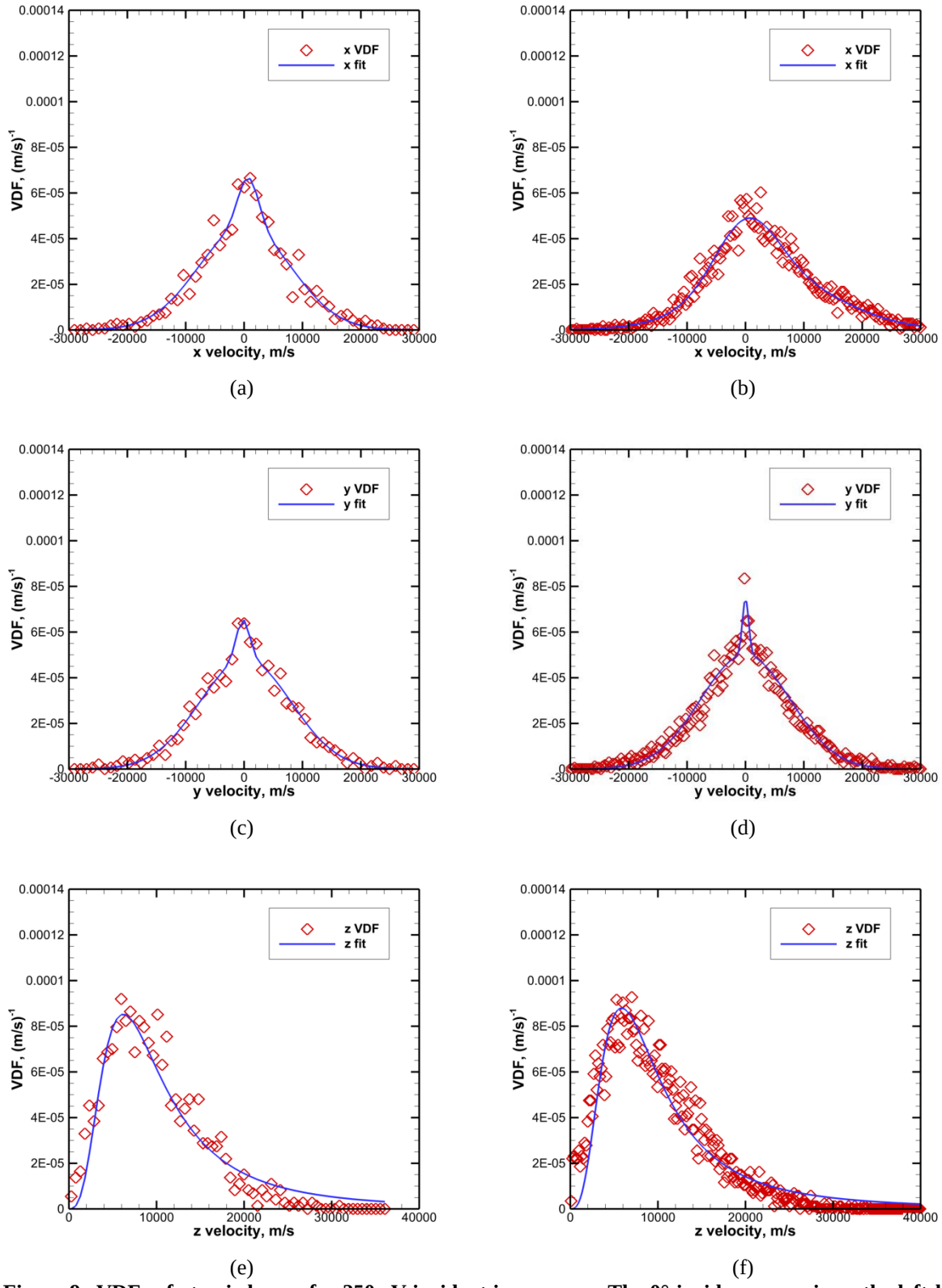

Figure 9. VDFs of atomic boron for 250 eV incident ion energy. The 0° incidence case is on the left-hand side of the page and the 45° incidence case is on the right-hand side.

The Sigmund-Thompson distributions fitted to the VDFs in z can be used to compare the results of the MD model to experimental measurements. The specific parameter of interest is the binding energy E_b, which is easily computed from the fitting parameter v_b. Past studies have indicated that the binding energy is strongly dependent on material properties and only weakly dependent on the energy and incidence angle of an impacting ion.[7, 26] Table 8 shows the Sigmund-Thompson parameters for the boron VDFs in the z direction. The computed binding energies have an average of 1.8 eV and do not seem to show any trends with ion energy or incidence angle. LIF measurements of sputtered boron by Tao[7] give a binding energy of about 4.8 eV, though those measurements were limited to sputtering of hBN by argon ions at a minimum energy of 300 eV and xenon ions at a minimum energy of 1200 eV. Hence, there is a clear discrepancy in the energy ranges studied in this work and those examined using LIF. In addition, there is a strong sensitivity of the binding energy to the value of m_{ST},[7] making a detailed comparison difficult without more data.

Table 8. Sigmund-Thompson parameters for VDFs of atomic boron in the z direction.

Ion energy	Ion incidence	m_{ST}	v_b	E_b
100 eV	0°	0.0	5200 m/s	1.5 eV
	45°	0.0	5400 m/s	1.6 eV
250 eV	0°	0.0	6200 m/s	2.2 eV
	45°	0.0	5800 m/s	1.9 eV

2. Diatomic nitrogen

VDFs of diatomic nitrogen are also computed. These VDFs are shown in Fig. 10 for the 100 eV vases and Fig. 11 for the 250 eV cases. Unlike atomic boron, diatomic nitrogen does not appear to obey the Sigmund-Thompson distribution in the z direction. Instead, the nitrogen VDFs along z are fitted using two flux-shifted Maxwell-Boltzmann distributions superimposed in the same manner as Eq. (12). A superposition is used because the VDFs shown in Figs. 10 and 11 show evidence of distinct populations of N_2: one low-temperature, low-energy population, and one high-temperature, high-energy population. Whereas atomic boron exhibits limited bimodal nature in its x and y velocity distributions, N_2 appears to have two discrete modes for each velocity component. To the authors' knowledge, there are no experimental data available on the behavior of sputtered N_2, so it is difficult to determine whether this is a physically realistic phenomenon. Assuming it is realistic, it is possible that the two populations emerge as a result of different sputtering mechanisms. Betz[26] distinguishes between three different sputtering mechanisms: single knock-on, linear collision cascade, and spike regime sputtering. The factor differentiating these mechanisms is the collisionality of the system during the sputtering event. For xenon ions with a few hundred electron volts of energy, single knock-on and linear cascade events are most likely. Single knock-on events are characterized by very short collision sequences, e.g. an ion imparting kinetic energy to an atom or molecule at a surface, causing it to be ejected from the lattice. Linear cascade events are characterized by a longer sequence of elastic collisions that eventually breaks the binding energy of an atom or molecule, causing it to be ejected from the system. It seems plausible that a bombarding ion of a given energy and incidence angle would transfer more of its kinetic energy to a single particle in a single knock-on event than in a linear collision cascade. Hence, repeated impacts at the same energy may result in a high-energy single knock-on population and a low-energy linear cascade population, both of which will be represented in the overall population of sputtered particles.

IV. Conclusions and future work

Presented in this work was an updated molecular dynamics model for the sputtering of hexagonal boron nitride by energetic xenon ions built with the open-source MD code HOOMD-blue. Graphics processing units were used to accelerate the MD computations by orders of magnitude, allowing long-term simulations that were intractable in past efforts. The improved model was used to compute total and differential sputter yields of hBN, as well as velocity distribution functions for the atomic boron and diatomic nitrogen present in the sputtering products. The cases simulated included ion energies of 100 and 250 eV and incidence angles of 0° and 45°. It was shown the total sputter yield has a strong, non-monotonic dependence ion fluence, first increasing as an amorphous layer of hBN is formed and then decreasing as the easily sputtered nitrogen is depleted from the lattice. Of the four cases simulated, only the 100 eV, 45° incidence case appears to have approached a steady state. Comparison to experimentally-measured sputter yields indicated that the 100 eV, 45° incidence case agrees well with mass loss measurements performed in the past. The computed differential sputter yields were well-described by a modified Zhang function, with RMS errors of 4–6% of the total yield between the computed and fitted contours. For the normally-incident cases, an azimuthally symmetric differential sputter yield profile was found, as is predicted by theory and observed in experiments. At 45° incidence, a clear preference towards forward sputtering was found. Analysis of the composition of the sputtering products indicated that boron is typically sputtered in its monatomic form whereas nitrogen is typically sputtered in the form of N_2. Computed VDFs of boron were well-described by a superposition

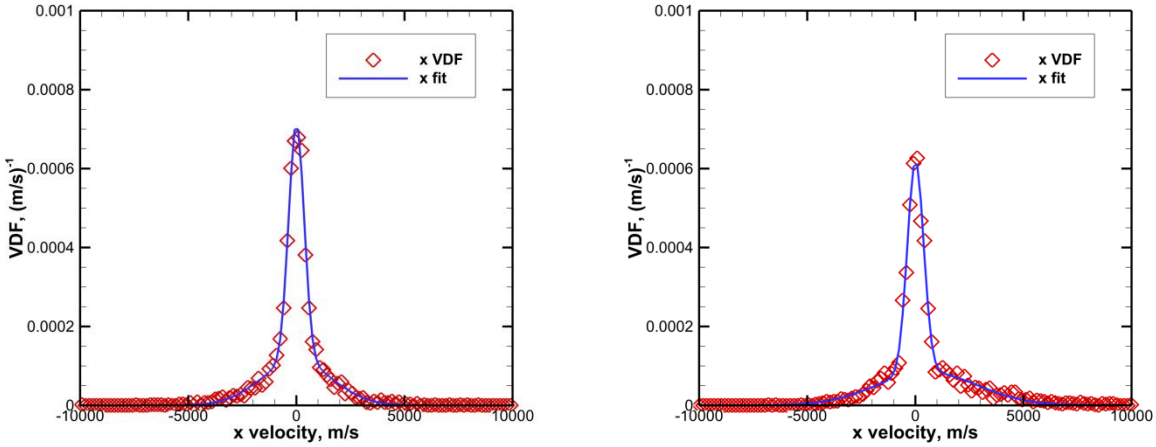

(a)

(b)

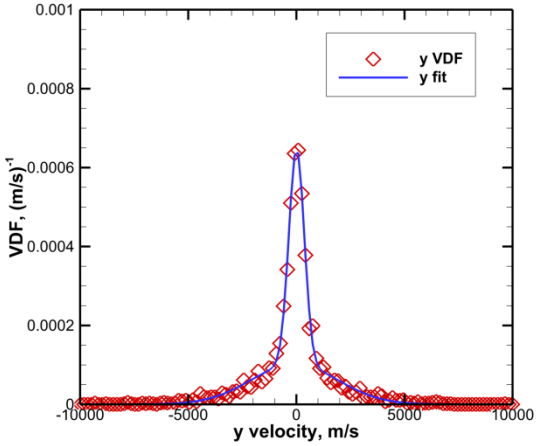

(c)

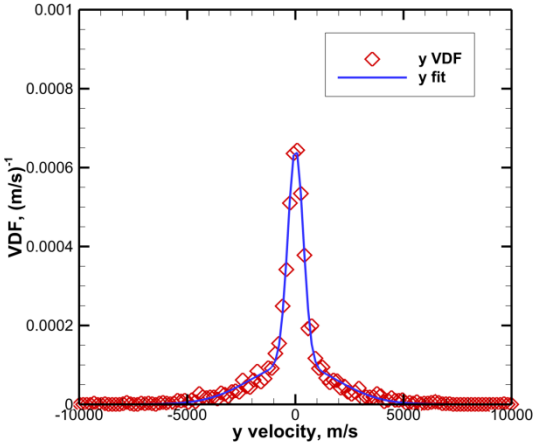

(d)

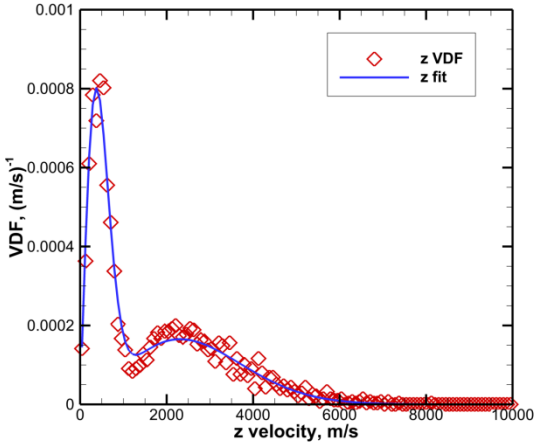

(e)

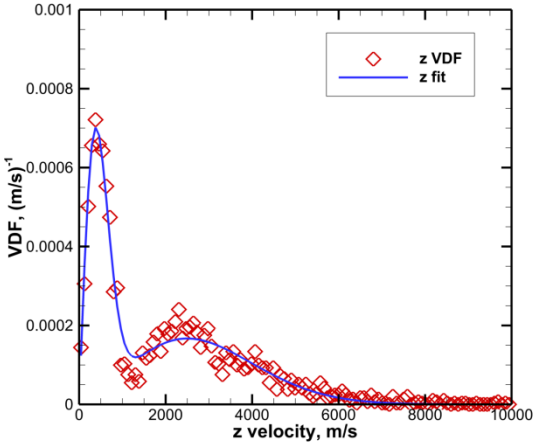

(f)

Figure 10. VDFs of diatomic nitrogen for 100 eV incident ion energy. The 0° incidence case is on the left-hand side of the page and the 45° incidence case is on the right-hand side.

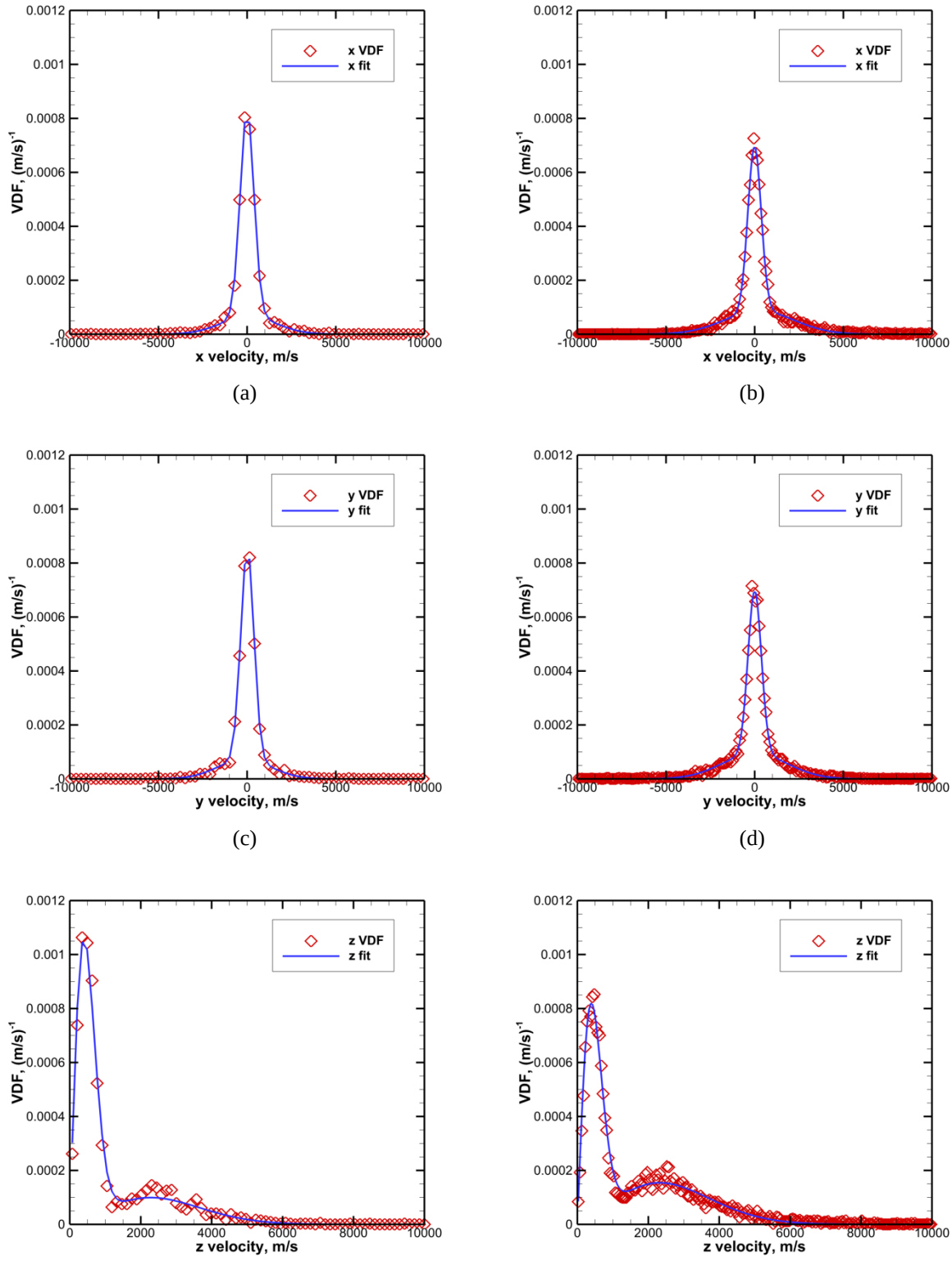

Figure 11. VDFs of diatomic nitrogen for 250 eV incident ion energy. The 0° incidence case is on the left-hand side of the page and the 45° incidence case is on the right-hand side.

of two Maxwell-Boltzmann distributions along axes parallel to the hBN surface and by the Sigmund-Thompson distribution in the direction normal to the surface. Comparison of the computed binding energies for boron in hBN to LIF measurements suggested that the MD model may be underestimating the binding energy, though the ion species and ion energies represented in the simulations and experiment differed widely. The computed VDFs for nitrogen exhibited a strong bimodal nature and were best described by superimposed Maxwell-Boltzmann distributions along the directions parallel to the hBN surface and by a superposition of flux-shifted Maxwell-Boltzmann distributions along the surface normal.

The clear step forward for this work is to simulate more sputter yield cases to a steady state. In particular, it would be valuable to simulate more cases for which there are experimental data available in order to better validate the models ability to compute total sputter yields. Such simulations will also provide differential sputter yield and VDF data that could be used to validate the model. Before doing so, however, the importance of the B–B interactions must be determined. It is clear that interactions between boron atoms become more common as nitrogen is depleted from the domain. Even if running long-term simulations using Albe's original coefficients proves to be intractable, it will be beneficial to know the consequences of using the modified coefficients.

Acknowledgments

This work was supported with the funding of a NASA Space Technology Research Fellowship, NASA grant #NNX11AM64H.

The authors would like to thank Dr. Joshua A. Anderson for his help in implementing the Albe potential in HOOMD-blue.

References

[1]Garnier, Y., Viel, V., Roussel, J.-F., and Bernard, J., "Low-energy xenon ion sputtering of ceramics investigated for stationary plasma thrusters," *Journal of Vacuum Science and Technology A*, Vol. 17, No. 6, 1999, pp. 3246–3254.

[2]Kim, V., Kozlov, V., Semenov, A., and Shkarban, I., "Investigation of the Boron Nitride based Ceramics Sputtering Yield Under its Bombardment by Xe and Kr ions," *27th International Electric Propulsion Conference*, Pasadena, California, USA, 2001.

[3]Yalin, A., Surla, V., Farnell, C., Butweiller, M., and Williams, J., "Sputtering studies of multi-component materials by weight loss and cavity ring-down spectroscopy," *42nd AIAA/ASME/SAE/ASEE Joint Propulsion Conference & Exhibit*, Sacramento, California, USA, 2006.

[4]Abashkin, V., and Gorshkov, O., "Analysis of Ceramic Erosion Characteristic in Hall-Effect Thruster with Higher Specific Impulse," *30th International Electric Propulsion Conference*, Florence, Italy, 2007.

[5]Rubin, B., Topper, J., and Yalin, A., "Total and differential sputter yields of boron nitride measured by quartz crystal microbalance," *Journal of Physics D: Applied Physics*, Vol. 42, Oct. 2009.

[6]Yim, J. T., Falk, M. L., and Boyd, I. D., "Modeling low energy sputtering of hexagonal boron nitride by xenon ions," *Journal of Applied Physics*, Vol. 104, No. 123507, 17 Dec. 2008.

[7]Tao, L., and Yalin, A., "LIF Velocity Measurement of Sputtered Boron Atoms from Boron Nitride Target," *46th AIAA/ASME/SAE/ASEE Joint Propulsion Conference & Exhibit*, Nashville, Tennessee, USA, July 2010.

[8]Plimpton, S., "Fast parallel algorithms for short-range molecular dynamics," *Journal of Computational Physics*, Vol. 117, 1995, pp. 1–19.

[9]Berendsen, H. J. C., Spoel, D. Van Der, and Drunen, R. Van, "GROMACS: A message-passing parallel molecular dynamics implementation," *Computer Physics Communications*, Vol. 91, Sep. 1995, pp. 43–56.

[10]Phillips, J. C., Braun, R., Wang, W., Gumbart, J., Tajkhorshid, E., Villa, E., Chipot, C., Skeel, R. D., Kalé, L., and Schulten, K., "Scalable molecular dynamics with NAMD.," *Journal of computational chemistry*, Vol. 26, Dec. 2005, pp. 1781–802.

[11]Todorov, I. T., Smith, W., Trachenko, K., and Dove, M. T., "DL_POLY_3: new dimensions in molecular dynamics simulations via massive parallelism," *Journal of Materials Chemistry*, Vol. 16, 2006, pp. 1911–1918.

[12]Anderson, J. A., Lorenz, C. D., and Travesset, A., "General purpose molecular dynamics simulations fully implemented on graphics processing units," *Journal of Computational Physics*, Vol. 227, No. 10, May 2008, pp. 5342–5359.

[13]Nickolls, J., Buck, I., Garland, M., and Skadron, K., "Scalable parallel programming with CUDA," *ACM Queue*, 2008.

[14]Albe, K., Möller, W., and Heinig, K., "Computer simulation and boron nitride," *Radiation Effects and Defects in Solids*, Vol. 141, Jun. 1997, pp. 85–97.

[15]Albe, K., and Möller, W., "Modelling of boron nitride: Atomic scale simulations on thin film growth," *Computational materials science*, Vol. 10, 1998, pp. 111–115.

[16]Los, J., and Fasolino, A., "Intrinsic long-range bond-order potential for carbon: Performance in Monte Carlo simulations of graphitization," *Physical Review B*, Vol. 68, Jul. 2003, p. 024107.

[17]Ziegler, J. F., Biersack, J. P., and Littmark, U., *Stopping and Ranges of Ions in Solids*, Pergamon Press, 1985.

[18]O'connor, D., and Biersack, J., "Comparison of theoretical and empirical interatomic potentials," *Nuclear Instruments and Methods in Physics Research B*, Vol. 15, 1986, pp. 14–19.

[19]Lehtinen, O., Dumur, E., Kotakoski, J., Krasheninnikov, a. V., Nordlund, K., and Keinonen, J., "Production of defects in hexagonal boron nitride monolayer under ion irradiation," *Nuclear Instruments and Methods in Physics Research Section B: Beam Interactions with Materials and Atoms*, Vol. 269, Jun. 2011, pp. 1327–1331.

[20]Humphrey, W., Dalke, A. and Schulten, K., "VMD - Visual Molecular Dynamics", *Journal of Molecular Graphics*, Vol. 14, 1996, pp. 33-38.

[21]Berendsen, H. J. C., Postma, J. P. M., van Gunsteren, W. F., DiNola, A., and Haak, J. R., "Molecular dynamics with coupling to an external bath," *The Journal of Chemical Physics*, Vol. 81, Oct. 1984, pp. 3684–3690.

[22]Sun, Q., and Boyd, I. D., "Evaluation of Macroscopic Properties in the Direct Simulation Monte Carlo Method," *Journal of Thermophysics and Heat Transfer*, Vol. 19, Jul. 2005, pp. 329–335.

[23]Zhang, Z., and Zhang, L., "Anisotropic angular distribution of sputtered atoms," *Radiation Effects and Defects in Solids*, vol. 159, May. 2004, pp. 301–307.

[24]Yalin, A. P., Williams, J. D., Surla, V., and Zoerb, K. A., "Differential sputter yield profiles of molybdenum due to bombardment by low energy xenon ions at normal and oblique incidence," *Journal of Physics D: Applied Physics*, Vol. 40, May. 2007, pp. 3194–3202.

[25]Thompson, M. W., "II. The energy spectrum of ejected atoms during the high energy sputtering of gold," *Philosophical Magazine*, Vol. 18, No. 152, 1968, pp. 377–414.

[26]Betz, G., and Wien, K., "Energy and angular distributions of sputtered particles," *International Journal of Mass Spectrometry and Ion Processes*, vol. 140, 1994, pp. 1–110.

[27]Yamamura, Y., "Theory of sputtering and comparison to experimental data," *Nuclear Instruments and Methods in Physics Research*, vol. 194, 1982, pp. 515–522.

[28]Zhang, L., and Zhang, Z., "Anisotropic energy distribution of sputtered atoms induced by low energy heavy ion bombardment," *Radiation Effects & Defects in Solids*, vol. 160, Aug. 2005, pp. 337–347.